ACS APPLIED MATERIALS & INTERFACES

Research Article

www.acsami.org

Controlled Photocatalytic Growth of Ag Nanocrystals on Brookite and Rutile and Their SERS Performance

Tian-Long Guo,[†,‡] Ji-Guang Li,[*,†,‡] De-Hai Ping,[§] Xudong Sun,[*,†] and Yoshio Sakka[‡]

[†]Key Laboratory for Anisotropy and Texture of Materials, School of Materials and Metallurgy, Northeastern University, Shenyang 110819, China

[‡]Advanced Materials Processing Unit, National Institute for Materials Science, Namiki 1-1, Tsukuba, Ibaraki 305-0044, Japan

[§]High Temperature Materials Unit, National Institute for Materials Science, 1-2-1 Sengen, Tsukuba, Ibaraki 305-0047, Japan

Supporting Information

ABSTRACT: Ag nanocrystals (NCs) were photocatalytically grown on the surfaces of brookite and rutile nanocrystals, respectively, and their surface-enhanced Raman scattering (SERS) performance was evaluated. The resultant Ag NCs exhibit different morphologies owing to the different photocatalytic capabilities of the two types of TiO_2 under otherwise identical synthetic conditions. The effects of $AgNO_3$ concentration, UV irradiation time, and UV light power on the morphology evolution and growth kinetics of the Ag NCs were systematically investigated. Moreover, PVP was found to serve as both a reductant and a capping agent in the photocatalytic reaction systems, and its presence allows morphological control of the Ag NCs. A proper amount of PVP was confirmed to favor Ag nanoplates of larger sizes and to produce SERS substrates of substantially better performance.

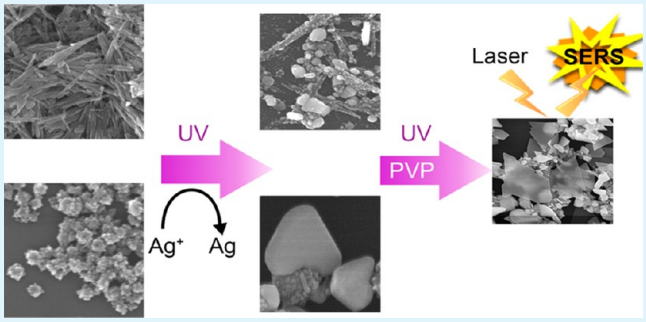

KEYWORDS: *silver nanocrystals, titania, photocatalysis, poly(vinylpyrrolidone) (PVP), surface-enhanced Raman scattering*

1. INTRODUCTION

As a highly sensitive and reliable analytical tool, surface-enhanced Raman scattering (SERS) has been widely studied since it was first reported by Fleischmann et al. in 1974.[1−6] It is commonly believed that the localized electromagnetic (EM) effect and chemical effect both contribute to the enhancement of Raman signals, and the former dominates the total SERS enhancement, especially on rough surfaces of group 11 metals (Cu, Ag, and Au).[7,8] Among these metals, silver is particularly favorable because of its high electrical and thermal conductivities. In addition, the optical constant of Ag provides the highest SERS efficiency in the visible-light region. In practice, when the target molecules are adsorbed around a suitable gap between the neighboring metal particles (hot spots), the Raman signal will be amplified 10^3−10^{11} times.[9−16] On the basis of this phenomenon, the generation of various substrates suitable for SERS has been attempted, such as aggregated colloids,[9,10] metallic film over nanospheres (MFONs),[11,12] particles in wells,[13,14] and nanofingers.[15,16]

Brookite (orthorhombic), rutile (tetragonal), and anatase (tetragonal) are three polymorphs of crystalline titania (TiO_2). As an *n*-type semiconductor caused by oxygen deficiency,[17] TiO_2 as a photocatalyst has received much attention over recent decades because of its high photo-activity, low cost, and good chemical and thermal stabilities.[18−20] TiO_2 substrate also has a feasible potential for use in a SERS application because of the charge transfer (CT) from TiO_2 to the adsorbed molecule.[21] To combine the CT effect from TiO_2 and the EM effect from noble metals,[22] TiO_2 has been used for the deposition of metal nanocrystals (NCs) for SERS.[23] The deposition methods that have been reported so far mainly include sputtering,[24] electrochemical deposition,[25] thermal deposition,[26] and UV/visible photocatalytic deposition.[27,28] In the photocatalytic-deposition technique, it was reported that the {001} facets of anatase are especially reactive.[29,30] The different crystal planes of TiO_2 have average surface energies in the order $\gamma\{110\}$ (1.09 J m^{-2}) > $\gamma\{001\}$ (0.90 J m^{-2}) > $\gamma\{100\}$ (0.53 J m^{-2}) > $\gamma\{101\}$ (0.44 J m^{-2}); hence, the enhanced exposure of the more reactive {110} and {001} facets may be responsible for raising the photocatalytic efficiency from 48.1 to 82.5%.[31] Ye et al. very recently reported a facile synthesis of anatase crystals with over 90% exposure of specifically selected facets free from contamination of any organic capping surfactants. With this, they were able to evaluate the photocatalytic reduction/oxidation efficiencies of the different anatase facets and found an order of {001} > {101} > {010}.[32] Aside from the {100} faceted anatase cuboids and rods, anatase nanosheets with 95% of {100} exposure were reported by Xu et

Received: September 17, 2013
Accepted: December 19, 2013
Published: December 19, 2013

al. to be of high photocatalytic reactivity.[33] TiO_2 nanocrystals of tunable crystal forms and facets were also attained by anion-assisted synthesis, and photocatalytic investigation again showed that the activity is both dependent on the type of TiO_2 and facet exposure.[34] Dense TiO_2 thin films have been prepared for photocatalytic synthesis of homogeneously distributed Ag NCs for SERS.[35] It was shown that, via surface modification, the photo-response of TiO_2 can be tuned from the UV to visible-light regions.[36] In all of these previous studies, however, phase-pure brookite decorated by Ag NCs for SERS has not been addressed, largely because of the difficulties encountered in synthesizing phase-pure brookite as compared with anatase and rutile. We have developed synthetic techniques that yield pure brookite as either discrete nanoplates or monodispersed spheres composed of nanoplates, and excellent photocatalytic capabilities were demonstrated for the decomposition of formaldehyde and methyl orange.[37,38] There has also been a report showing that brookite exhibits good potential in photocatalytic silver deposition, but no attempts were made to manipulate the Ag morphology for SERS applications.[39]

In this article, both pure brookite and rutile NCs were synthesized and used as the substrates to deposit Ag NCs via photocatalysis. The growth kinetics of Ag on each substrate was systematically investigated, and morphology control of the resultant Ag NCs was achieved via a careful design of deposition parameters. The effects of poly(vinylpyrrolidone) (PVP) as an additive are also discussed in detail. Finally, the SERS performance of the resultant Ag NCs was evaluated via detection of Rhodamine 6G (R6G) and correlated to the crystal morphologies of Ag.

2. EXPERIMENTAL METHODS

2.1. Chemicals and Materials. Titanium trichloride solution ($TiCl_3$, 20%), nitric acid (HNO_3, 65%), urea ($CO(NH_2)_2$, reagent grade), silver nitrate ($AgNO_3$, 99.9%), ethanol (C_2H_5OH, 99.5%), methyl orange ($C_{14}H_{14}N_3NaO_3S$, reagent grade), and Rhodamine 6G (R6G, $C_{28}H_{31}ClN_2O_3$, reagent grade) were all purchased from Wako Pure Chemical Industries (Osaka, Japan). Poly(vinylpyrrolidone) (PVP, $(C_6H_9NO)_x$, M_w = 10 000 g mol^{-1}) was purchased from Sigma-Aldrich, Inc. (MO, USA). Milli-Q purified water was used throughout the experiments.

2.2. Synthesis, Characterization, and Photocatalytic Evaluation of Titania Nanocrystals. Both the brookite and rutile types of TiO_2 were synthesized as reported previously.[37,38] Characterization of the powders was achieved by X-ray diffractometry (XRD, model RINT 2200 V/PC, Rigaku Co., Tokyo, Japan) operated at 40 kV/40 mA with nickel-filtered Cu Kα radiation and a scanning speed of 0.5° 2θ/min. Particle morphology was observed via field-emission scanning electron microscopy (FE-SEM, model S-5000, Hitachi Co. Ltd., Tokyo) operated at 10 kV.

2.3. Photocatalytic Growth of Silver Nanostructures, Characterization, and SERS Measurements. The synthesized TiO_2 powder (1 mg) was added in ethanol (10 mL) and then fully dispersed via ultrasonication at 120 W for 15 min. The resultant suspension was dripped onto a ~4 × 4 mm^2 silicon wafer slide. After drying in air, the slide was immersed in 3 mL of a base solution (0.05–0.1 M of $AgNO_3$ or $AgNO_3$/PVP mixture) contained in a petri dish (36 mm in diameter). The PVP content was varied from 3 to 200 wt % (mass ratio against $AgNO_3$). The dish was then placed under UV irradiation (1, 5, 10, and 20 mW cm^{-2}) for various periods of time (10, 30, 45, and 60 min). The UV light was generated by a 200 W high-stability mercury–xenon lamp (A type, San-Ei Electric Co., Ltd., Osaka, Japan) using a UV-curing system (model UVF-204S, San-Ei Electric Co., Ltd.). After irradiation, the slide was gently washed with water and ethanol followed by air-drying. Sample morphologies were observed via FE-SEM operated at 10 kV and transmission electron microscopy (TEM, model FEM-3000F, JEOL Ltd., Tokyo, Japan) under an acceleration voltage of 300 kV. The TEM image was further processed by Gatan Digital Micrograph software. UV–vis absorption spectra were measured with a spectrophotometer (model V-560, JASCO Co. Ltd.). Photoluminescence (PL) excitation and emission spectra were recorded with a fluorospectrophotometer (model FP-6500, JASCO Co. Ltd.) equipped with a 150 W xenon lamp as the excitation source. AFM images were acquired with the tapping mode at a scanning rate of 1 Hz (NanoScope IIIa multi mode AFM, Veeco Instruments Inc., NY, USA). Raman spectra were taken under ambient conditions on a micro-Raman spectrophotometer (model Jobin Yvon T64000, Horiba Co. Ltd., Tokyo, Japan) with a 170 μW Ar^+ laser (514 nm) as the excitation source. The acquisition time was 20 s, and the signal was acquired under two accumulations. The laser spot was ~1 μm^2 under a 90× air objective lens. Samples for SERS evaluation were prepared by immersing the silicon slide in a R6G solution (1 μM for Ag-brookite, 0.1 mM for Ag-rutile, and 0.1 M for bare quartz) for 10 min followed by air-drying at 50 °C.

3. RESULTS AND DISCUSSION

3.1. Characterization of the TiO_2 Nanopowders. Both rutile and brookite powders were synthesized as pure phases but with distinctly different particle morphologies, as shown in Figure 1. The rutile crystals are nanorods with diameters of

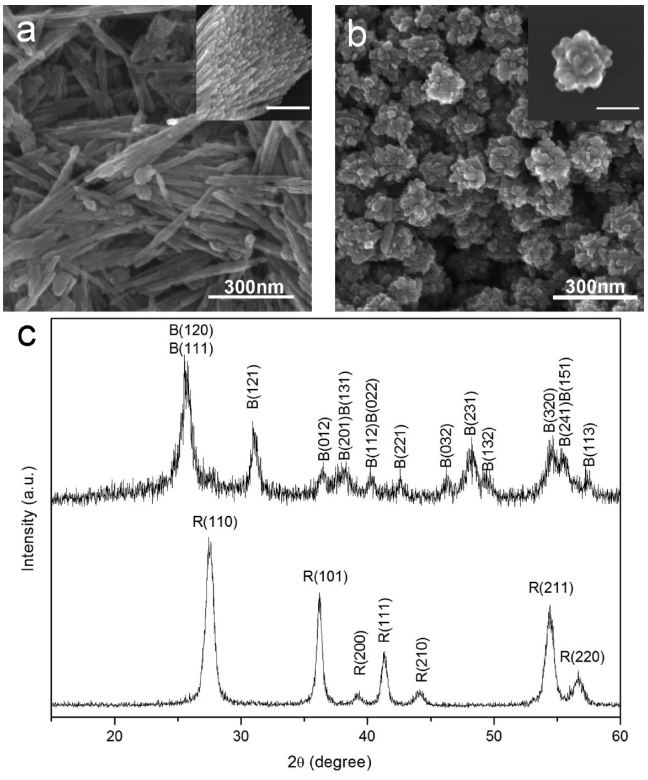

Figure 1. FE-SEM images of the as-made rutile (a) and brookite (b) powders. The scale bars in the insets represent 100 nm. (c) XRD patterns of the two types of TiO_2.

~20 nm and lengths of up to ~400 nm. Under the chosen $TiCl_3$ concentration (0.6 M), the nanorods are not fully separated, and bundle-like aggregates are occasionally observable (Figure 1a, inset). The brookite particles are roughly monodispersed, round in shape, and have fairly uniform diameters of ~100–150 nm (Figure 1b). Each particle is composed of much finer (~10–20 nm) primary crystallites of the brookite-type TiO_2 and appears flowerlike (Figure 1b,

dx.doi.org/10.1021/am404027m | ACS Appl. Mater. Interfaces 2014, 6, 236–243

inset). All of these observations are in accordance with our previous reports.[37,38] XRD analysis (Figure 1c) confirmed that the two TiO_2 powders are phase-pure and of good crystallinity and can be well-indexed to rutile (JCPDS card no. 21-1276) and brookite (JCPDS card no. 29-1360), respectively. It was reported that brookite shows characteristic Raman scatterings at 128, 153, 247, 322, 366, and 636 cm^{-1}, whereas rutile is at 143, 235, 447, and 612 cm^{-1}. Our Raman analyses of the two TiO_2 powders (Figure S1, Supporting Information) are in good accordance with the literature[40] and further confirm the phase purity revealed by XRD.

3.2. Ag NCs Grown on Brookite. As an fcc material, Ag NCs have a naturally designed growth route to follow. In general, the Ag seeds (nuclei) coexist as single crystals (defect free) and crystals with singly or multiply twinned structures in a typical synthesis. Once the seed is formed, further addition of Ag atoms can lead to size growth. It is well-known that crystal formation is dominated by either thermodynamic or kinetic control. Under thermodynamic control, the crystal tends to retain the most stable form through minimizing the total interfacial free energy of the system with a fixed volume. Because the low-index crystallographic facets of {111}, {100}, and {110} have increasing surface energies,[41] the single-crystal seeds under thermodynamic control are thus expected to take octahedral or tetrahedral shapes, which allows maximization of the {111} facets to minimize the surface energy. By precisely manipulating the relative growth rate along the ⟨111⟩ and ⟨100⟩ directions, further crystal growth will result in cubes, octahedrons, or cuboctahedrons covered with a mixture of the {111} and {100} facets.[42] Moreover, octagonal rods and rectangular bars may be formed from the cuboctahedral and cubic seeds, respectively, if uniaxial growth is induced.[43] Singly or multiply twinned seeds, each of which has at least one twin defect (that is, a single atomic layer in the form of a (111) mirror plane), also follow the growth pattern of single-crystal seeds to minimize the total interfacial free energy by exposing a mixture of the {111} and {100} facets. Notice that as a defected crystal the twinned seed initially has a higher energy than the single-crystal one because of the strain energy caused by the loose packing of atoms along the mirror plane (a geometrical deficiency).[44−47] If the twinned seed is rapidly expanded during further size growth, then compensation of the total energy by maximization of the {111} facets is inadequate, as revealed by theoretical calculations.[48−51] As a result, the highly strained twinned seeds will transform into single crystals. Only if the seed size is controlled within a small region and the reaction rate is considerably slow can the singly twinned and five-fold twinned seeds evolve into the right shapes of bipyramid and decahedron/icosahedron, respectively. Additionally, uniaxial growth of the bipyramid and decahedron may lead to nanobeam and pentagonal nanorod, respectively.

Under kinetic control, the relatively high reaction rate will cause the Ag atoms to form seeds with stacking faults,[52,53] and the crystal shape can deviate from that favored by thermodynamics. Considering the relatively large surface area relative to a polyhedral seed of a given volume and the strain energy caused by defects, the total free energy of a plate seed is incredibly high even with the coverage of {111} facets. To obtain platelike crystals, considerably fast seed formation and growth would thus be needed.

To observe the growth patterns of Ag NCs on TiO_2 and to achieve the highest SERS enhancement factor (EF), UV light power, UV irradiation time, and $AgNO_3$ concentration were set as variables. Figure 2a−d reveals the time-course evolution of Ag NCs on brookite. Ag nanoplates and polyhedrons (Figure 2a, arrow) can be found in each image, but with the latter dominating the morphology. As aforementioned, Ag platelets are originated from crystal seeds having stacking faults, and considerably fast nucleation and growth are required for their formation. These are allowed primarily by the high reduction power of brookite. The Ag polyhedrons are formed via a simultaneous growth of the different crystal planes. As irradiation time increases, the crystal size increases from upwards of ∼30 (Figures 2a) to ∼250 nm (Figure 2d).

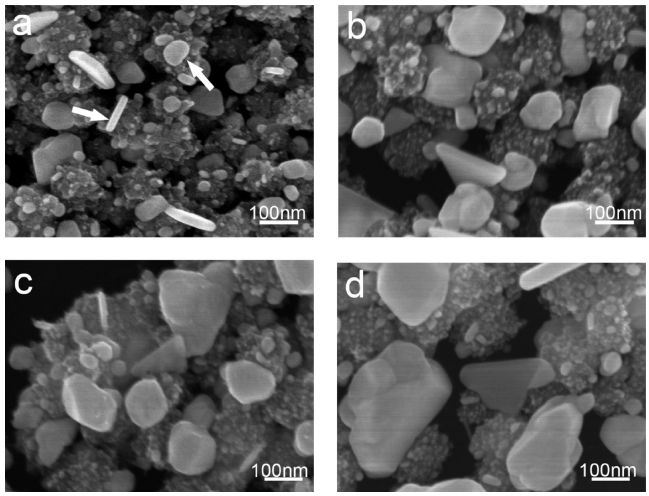

Figure 2. FE-SEM images of the Ag NCs−brookite substrates grown with 0.1 M $AgNO_3$ under 5 mW cm^{-2} UV irradiation for 10 (a), 30 (b), 45 (c), and 60 min (d).

Figure 3 shows morphologies of the Ag−brookite substrates made with different UV power. It was noticed that Ag nanoplates gradually disappear as the UV power is increased (Figure 3a−d). It is obvious that increasing the UV power improves the reduction ability of brookite, which helps the Ag crystals to overcome the growth energy barriers for different facets and thus the Ag NCs gradually become exclusively

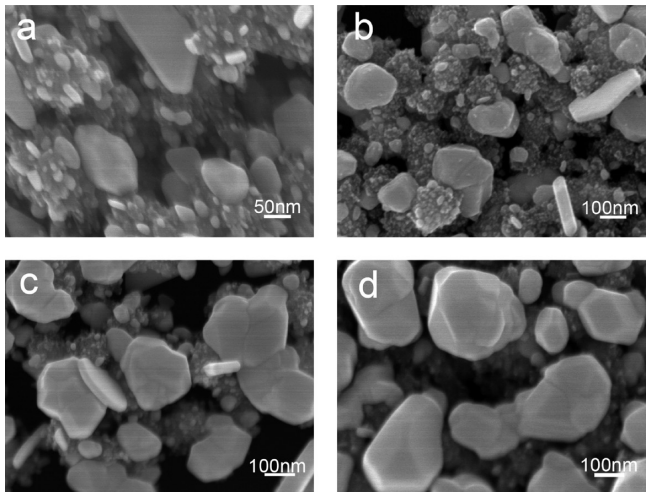

Figure 3. FE-SEM images of the Ag NCs−brookite substrates made with 0.1 M $AgNO_3$ and 45 min of UV irradiation under UV power of 1 (a), 5 (b), 10 (c), and 20 mW cm^{-2} (d).

shaped as polyhedrons. Crystal size was observed to increase with increasing UV power, from ~50−200 nm in Figure 3a−c to ~200−300 nm in Figure 3d.

3.3. Ag NCs Grown on Rutile. The same set of experiments was performed by changing the photocatalyst from brookite to rutile (Figure 4). It was noticed that the Ag

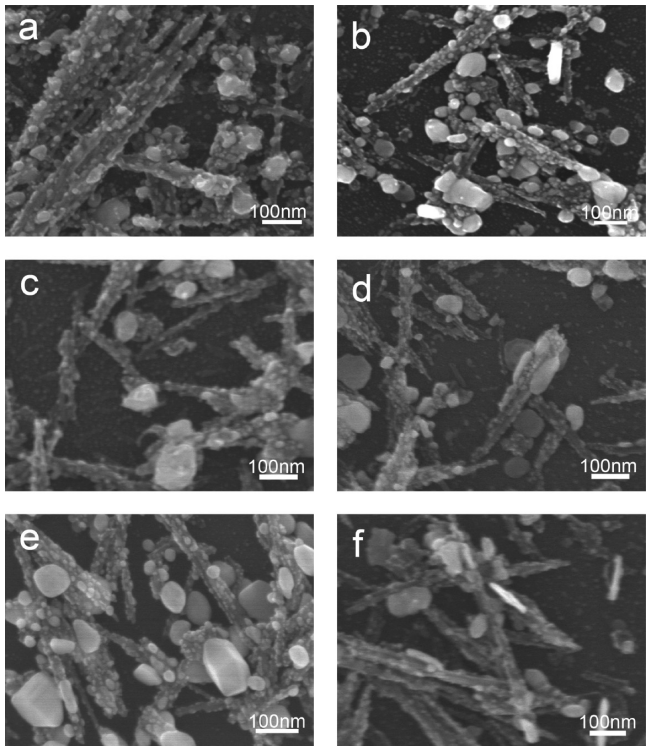

Figure 4. FE-SEM images of the Ag NCs grown on rutile (a−c) with 0.1 M $AgNO_3$ under 5 mW cm^{-2} of UV for 30, 45, and 60 min, respectively; (d, e) with 0.1 M $AgNO_3$ for 45 min under 10 (d) and 20 $mWcm^{-2}$ (e) of UV, respectively; (f) with 0.05 M $AgNO_3$ under 5 mW cm^{-2} of UV for 45 min.

NCs tend to grow along the rutile nanorods (Figure 4a), and with increasing time those at the tips and junctions of the nanorods grow significantly faster than the ones attached on the main body (Figure 4b,c). This is primarily because the electrons generated from TiO_2 under UV irradiation gather more easily at the tips and junctions and the electron-hole pairs are more easily separated against recombination at these interfaces (charge separation), thus leading to a higher usage of the electrons in the reduction process and higher reduction power at these sites. Figure 4b,d,e reveals that increasing UV power yields significantly more polyhedral crystals of larger sizes, following the trend observed in the case of brookite (Figure 3). Decreasing the $AgNO_3$ concentration from 0.1 to 0.05 M does not significantly affect the overall crystal morphology but leads to generally smaller crystals (comparing Figure 4, panels b and f). It is also noticeable from Figure 4f that the crystals tend to be separated from each other and have larger interspaces because of the lower nucleation density caused by the lower $AgNO_3$ concentration. Because of the relatively low photocatalytic ability of rutile compared with brookite (Figure S2),[38] the Ag NCs shown in Figure 4 are all significantly smaller than those made with brookite under otherwise identical conditions (Figures 2 and 3). Ag nanoplates are rarely observable in Figure 4 because crystal seeds having stacking faults are hardly formed under the low reduction power of rutile.

3.4. Mechanism of Ag Nucleation and Growth on TiO_2. As a semiconductor, TiO_2 has a band gap of around 3.0 eV, which corresponds to a wavelength of 413 nm. Irradiating TiO_2 with shorter-wavelength light (higher energy) will excite electrons from the valence band to the conduction band of TiO_2, leaving positively charged holes behind. Both the electrons and holes may migrate to crystallite surfaces to participate in chemical reactions. For the photocatalytic Ag deposition studied in this work, the Ag^+ ions in solution are reduced to Ag atoms on TiO_2 surfaces according to $Ag^+ + e^- \rightarrow Ag^0$. Further accumulation of Ag atoms will lead to the formation of transit Ag nuclei and stable nuclei and eventually to the growth of Ag nanocrystals. The transit Ag nuclei are very tiny clusters in the solution, which transform into stable ones when their size reaches a critical value through Ag atom accumulation. Further growth of these stable seeds results in the formation of Ag NCs. Different from the classical growth under thermodynamic equilibrium conditions, the shape of photocatalytically grown Ag NCs heavily depends upon the reduction power of the reaction system. With the fast electron generation by the more reactive brookite and under high UV power, the seeds with twinned defects/stacking faults preferentially grow into the less stable (higher surface energy) shapes of nanoplates. On the contrary, the Ag NCs grown with rutile and under low UV power tend to take the more stable form of polyhedrons. A longer reaction time promotes crystal growth and also helps to eliminate crystal defects to form more stable polyhedron crystal shapes. As shown by the previous experimental results, Ag substrates of intended crystal morphologies can be obtained through manipulating the Ag^+ concentration, UV light power, reaction time, and, in particular, the crystal structure of the TiO_2 photocatalyst.

3.5. Effects of PVP on Ag NCs Growth. It was reported that PVP as a capping agent is preferentially bounded with the {100} facets of Ag through its oxygen atom in the carbonyl group of C═O. This binding effect can drive additional atoms to other facets and thus reduces the growth rate along the ⟨100⟩ direction and makes the {111} facets disappear more quickly than the {100} ones. This preferential capping can result in Ag nanocrystals of peculiar shapes, such as nanocubes, octahedrons, and nanobars, and others for single-crystal seeds.[55−58] Moreover, PVP may act as a reductant to provide a reducing environment upon being heated in solution.[54,57] The role of PVP in photocatalytic reaction, however, has rarely been reported. To modify further the morphology of Ag NCs and to clarify the role of PVP in the TiO_2 photocatalytic system, PVP was introduced into a 0.1 M $AgNO_3$ solution, and experiments were performed with an irradiation time of 45 min and a UV power of 5 mW cm^{-2}. Figure 5 shows the morphology evolution of the Ag NCs with increasing PVP addition (3−200 wt %, mass ratio against $AgNO_3$). The sample made with 3 wt % PVP (Figure 5a) is dominated by Ag nanoplates and polyhedrons but has significantly more nanoplates when compared with those synthesized without PVP (Figure 2b). Moreover, increasing the PVP content to ~50 wt % produces more Ag nanoplates of larger sizes (Figure 5a−d). Further increasing the PVP content changes the dominant morphology from nanoplates to polyhedrons. It is also seen that the polyhedrons tend to have larger sizes at a higher PVP content. The significant effects of PVP can be more readily seen with rutile as the photocatalyst (Figure S3). That is, substantially

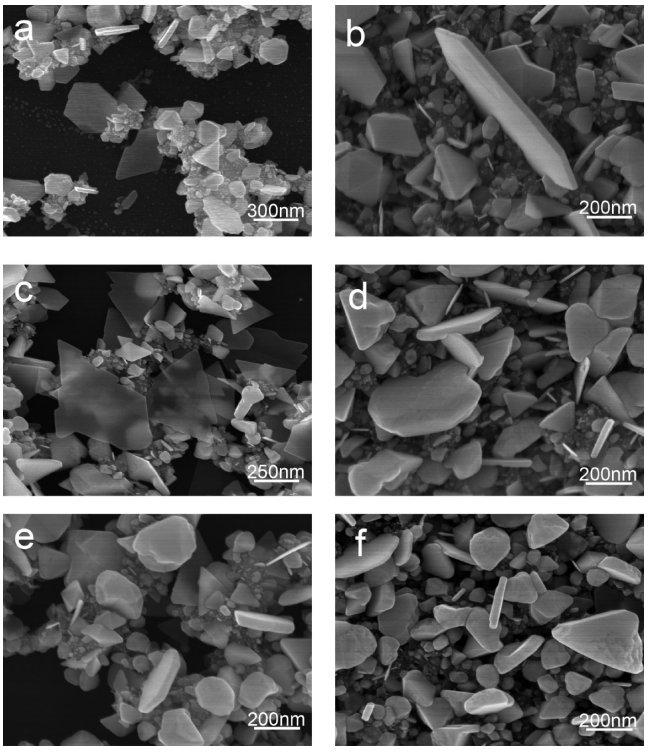

Figure 5. FE-SEM images of the Ag NCs grown on brookite and in the presence of 3 (a), 5 (b), 10 (c), 50 (d), 120 (e) and 200 wt % (f) of PVP (mass ratio against $AgNO_3$). The $AgNO_3$ concentration, UV power, and growth time were 0.1 M, 5 mW cm^{-2}, and 45 min, respectively.

more Ag nanoplates are formed with PVP addition up to ~50 wt %, which is in sharp contrast to the results obtained without PVP (Figure 4). Similar to the brookite case, the Ag crystals tend to transform from platelike to polyhedral at the even higher PVP contents of 120 and 200 wt %, and the crystal size tends to increase with increasing PVP addition. The above results thus suggest that PVP has profound effects on the growth pattern and growth kinetics of Ag crystals in the present photocatalytic systems.

Figure 6a exhibits the morphology of a Ag nanoplate synthesized with brookite in the presence of 10 wt % PVP (the

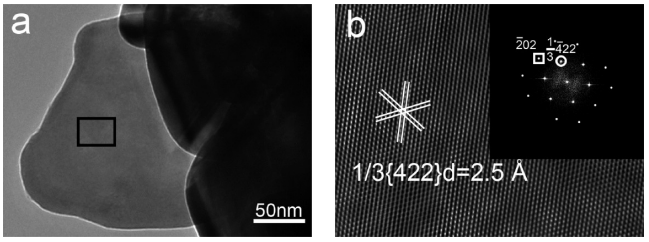

Figure 6. TEM analysis of the sample shown in Figure 5c. (a) Morphology of a Ag nanoplate and (b) IFFT image of the rectangle in panel a. The inset in panel b is the FFT analysis of lattice image.

same sample as in Figure 5c), and Figure 6b is the inverse fast Fourier transformation (IFFT) image of the rectangle in panel a recorded along the [111] zone axis. Analysis of the lattice image found a *d* spacing of ~2.5 Å, which can be ascribed to the 1/3{422} reflection of Ag. Fast Fourier transformation (FFT) analysis of the lattice image (the inset) yielded well-defined diffraction spots, suggesting that the nanoplate is single crystalline. The squared diffraction spot corresponds well to the {$\bar{2}$02} diffraction, implying that the surface of Ag nanoplate is covered by {111} facets. The circled spot is ascribed to the 1/3{$\bar{4}$22} diffraction, which is forbidden for the fcc material and is only observable from atomically flat surfaces of silver or gold nanocrystals.[59]

3.6. Roles of PVP and TiO_2 in the Photocatalytic System. To separate the roles of PVP and TiO_2 in the photocatalytic morphology evolution of Ag NCs, comparative experiments were performed under UV irradiation (5 mW cm^{-2}) for 45 min of (1) 10 mL of a 0.1 M $AgNO_3$ solution containing 100 wt % of dissolved PVP, (2) 10 mL of an aqueous solution containing 20 mg of PVP, and (3) 10 mL of an aqueous suspension containing 20 mg of dissolved PVP and 1 mg of brookite. PL and PLE analysis of solution (2) and the supernatant of (3) after UV irradiation yielded almost identical results (Figure S4), clearly indicating that the PVP molecules were not decomposed by the brookite catalyst under the adopted UV irradiation. The excitation and emission behaviors of PVP in water are not available to us in the literature, but the PLE band observed in the ~225−400 nm region and the PL band found in the ~425−600 nm region may be largely associated with the N- and O-containing functional groups in the PVP molecules. Solution (1) turned from colorless to yellowish after the UV irradiation, as seen from the appearance of the solution (Figure 7d, inset) and also from the UV−vis

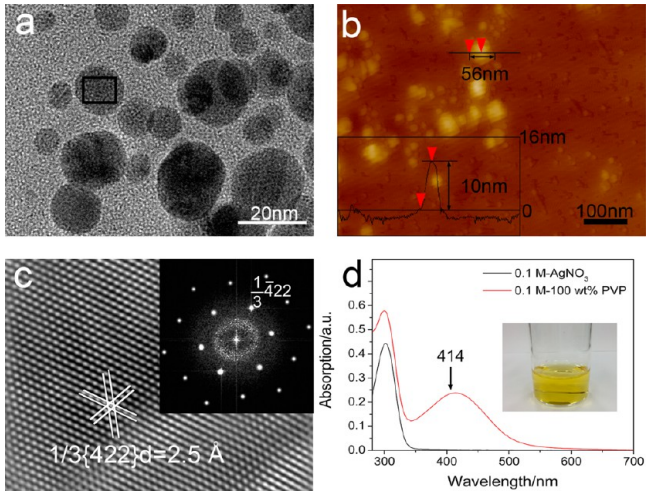

Figure 7. (a) TEM image of the Ag NCs obtained by UV irradiation (5 mW cm^{-2}) for 45 min of a 0.1 M $AgNO_3$ solution containing 100 wt % of PVP. (b) Tapping mode AFM topographic image and height profile of a Ag particle shown in panel a. (c) IFFT lattice image of the rectangle region shown in panel a. (d) UV−vis absorption spectra of a pure $AgNO_3$ solution (black line) and a $AgNO_3$/PVP mixed solution (red line) after UV irradiation. The inset in panel c is the FFT analysis of the lattice image and that in panel d is the appearance of the mixed solution after the UV irradiation (digital picture).

absorption spectrum (Figure 7d, red line). TEM analysis of the reaction product (after centrifugal separation and water washing) of solution (1) found rounded objects having diameters of ~20 nm (Figure 7a). The rather faint contrast of the TEM image may suggest that the particles are somewhat platelike rather than spheres. AFM analysis indeed found that some particles have a lateral size of ~56 nm but a maximum thickness of only ~10 nm (Figure 7b). Theoretical calculation indicated that the solution of 40 nm sized Ag nanospheres

dx.doi.org/10.1021/am404027m | ACS Appl. Mater. Interfaces 2014, 6, 236−243

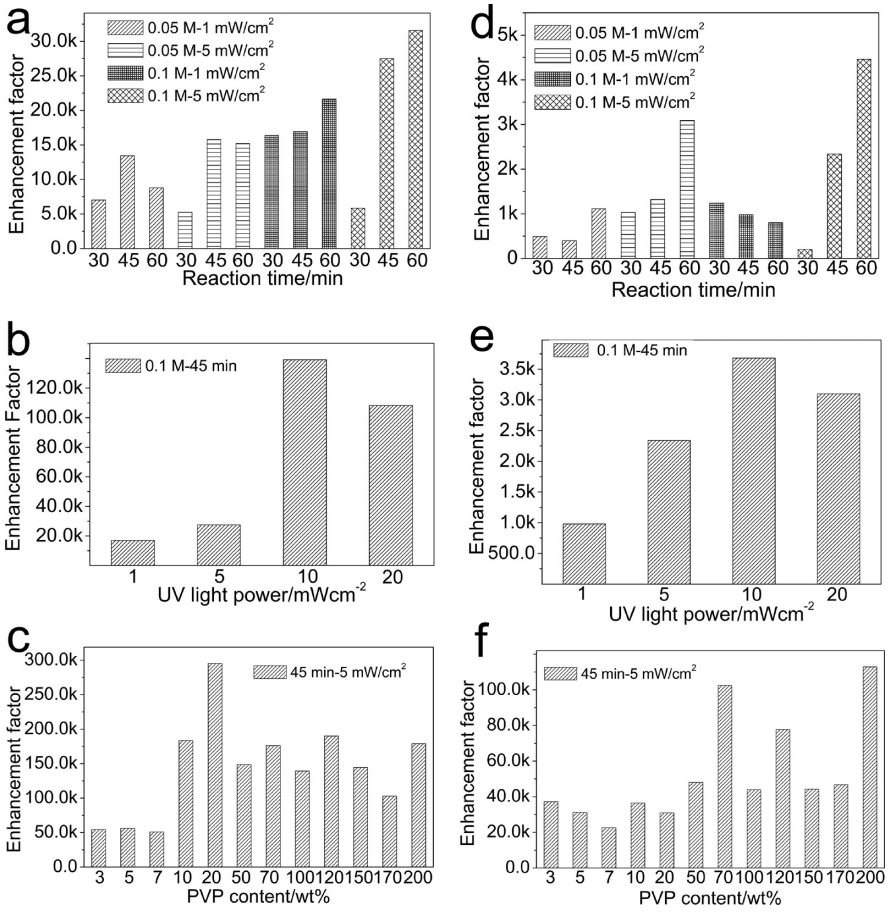

Figure 8. Comparison of the enhancement factor (EF) for various SERS substrates: (a–c) substrates grown on brookite and (d–f) substrates grown on rutile. The $AgNO_3$ concentration is 0.1 M for both panels c and f. The 1361 cm^{-1} Raman band of R6G was chosen for EF calculation.

absorbs blue light to produce a UV–vis absorption band at ~410 nm and hence appears yellow.[60] It can thus be said that the nanoplate-like Ag particles obtained in this work exhibit optical properties almost identical to the aforementioned nanospheres. The results of IFFT and FFT analyses of the rectangle region in Figure 7a highly coincide with those shown in Figure 6b. The roles of PVP and TiO_2 may thus be discussed as follows from the results of Figures 5–7: (1) PVP itself is a reductant for Ag^+ under UV irradiation and thus Ag nanoparticles are formed even in the absence of any TiO_2 photocatalyst (Figure 7a). The reducing power of PVP, however, seems limited because the PVP molecules oxidized by Ag^+ cannot recover to the neutral state without the presence of an electron donor. This would account for the tiny sizes of the Ag nanoparticles shown in Figure 7a. (2) PVP, in a proper amount, promotes the growth of Ag nanoplates (Figures 5, 7, and S3). As already mentioned, the PVP molecule is preferentially adsorbed on the {100} facets of Ag. The in situ reduction of Ag^+ to Ag by the bounded PVP under UV allows the {100} facets to grow faster and thus Ag nanoplates with a maximized exposure of the {111} facets result. The findings of this work are clearly different from those obtained when solely PVP acts as a capping agent. In the latter case, Ag nanocubes, octahedrons, or nanorods are preferentially formed.[55−58] In addition, the TiO_2 photocatalyst can furnish electrons to recover the PVP molecules oxidized by Ag^+ and thus higher reducing ability is attained for the systems containing both TiO_2 and PVP to yield significantly larger Ag nanoplates (Figures 5 and S3). (3) The amount of PVP significantly affects the shape evolution of Ag NCs, and nanoplates tend to change into polyhedrons when the PVP content is over 120 wt % (Figures 5e,f and S3e,f). This is because the preferential capping vanishes in the presence of significantly excessive PVP, and Ag polyhedrons are thus produced via a simultaneous growth (isotropic growth) of the different Ag facets.

The relationships between Ag NCs morphologies and processing parameters are summarized in Table S1.

3.7. SERS Tests of Ag NCs–TiO_2 Substrates. The SERS ability of the Ag/TiO_2 hybrid system was tested using Rhodamine 6G (R6G) as an analyte. The typical Raman spectra of R6G taken on the substrates shown in Figures 2d, 3c, and 5c are presented in Figure S5, from which it is seen that the R6G peaks can be well-identified in each case. The enhancement factor (EF) of the Raman signals was calculated using the following equation

$$\mathrm{EF} = (I_{\mathrm{SERS}}/I_{\mathrm{bulk}})(N_{\mathrm{bulk}}/N_{\mathrm{SERS}}) \quad (1)$$

where I_{SERS} and I_{bulk} represent the intensities of the 1361 cm^{-1} Raman peak of R6G adsorbed on the SERS substrate and bare quartz, respectively, and N_{bulk} and N_{SERS} are the number of surface adsorbed R6G molecules. The I value is the intensity of the 1361 cm^{-1} Raman peak relative to the left-hand tail of the spectrum baseline. Because the preparation procedures are the same for the Ag-deposited and bare substrates, N is assumed to be directly proportional to the concentration of R6G solution. Figure 8 shows the EFs of all of the tested samples calculated

dx.doi.org/10.1021/am404027m | ACS Appl. Mater. Interfaces 2014, 6, 236–243

by comparing the 1361 cm^{-1} Raman band intensity with that of 0.1 M R6G (Figure S6). It should be noted that the test point was randomly selected from the areas where Ag NCs exist. It can be seen that the samples compared in the same part of Figure 8 have roughly the same order of magnitude of their EF. Although there are deviations in the EF in each panel, the effects of the synthetic parameter can still be seen and are summarized as follows:

(1) Irradiation time (Figure 8a,d): increasing irradiation time tends to yield more and larger Ag NCs, leading to smaller interspaces among the Ag NCs and thus higher EFs;
(2) UV light power (Figure 8b,e): higher UV power elevates the reduction power of the reaction system and hence promotes nucleation and growth of Ag NCs. Generally, higher EFs are observed because of the decreased interspaces among the Ag NCs;
(3) $AgNO_3$ concentration (Figure 8a,d): under sufficient reduction power, more Ag^+ in the solution produces more Ag atoms for Ag nucleation/growth and thus generally higher EFs;
(4) PVP (Figure 8c,f): PVP acts as both a reductant and a capping agent. It is clear that the EFs are elevated by ~10−50-fold with the Ag NCs synthesized in the presence of PVP. The improved EFs result from the nucleation density and morphology changes of Ag by PVP. We confirmed by a separate study that the PVP molecules adsorbed on Ag surfaces do not contribute to the Raman signal enhancement of R6G (Figure S7).

The SERS activity of Ag/anatase composites, although not involved in this work, seems to have EFs comparable to or slightly higher than the best value of this work (~3.0×10^5; Figure 8c, 20 wt % of PVP). For example, the Ag/anatase nanofiber composites produced via electrospinning have EFs of around 5.0×10^5 (analyte: 4-mercaptopyridine),[61] and the Ag/*n*-anatase composite (*n*: nanotube), where Ag was sputtered on the *n*-anatase anodized from Ti foil, has an EF of about 10^6−10^7 (analyte: pyridine).[62] From the previous and current studies, it can be concluded that the overall morphology of Ag nanocrystals is the decisive factor affecting SERS performance, including crystallite size, crystal shape, number density (interspacing), and spatial distribution. The better SERS activity of Ag/*n*-anatase composite is primarily a result of its significantly higher number density of the sputtered Ag nanocrystallites.

4. CONCLUSIONS

A facile photochemical method was introduced in this work to grow Ag NCs for SERS applications. The resultant Ag NCs were found to exhibit different morphologies on brookite and rutile photocatalysts under otherwise identical reaction conditions owing to the different photocatalytic abilities of the two types of TiO_2. $AgNO_3$ concentration, UV power, and irradiation time all appreciably affect the growth kinetics and morphology of the Ag product. Increasing the $AgNO_3$ concentration leads to morphology changes from smaller nanoparticles (NPs) to nanoplates and then to larger polyhedrons and enhances crystal growth. UV power and UV irradiation time affect Ag NCs in the same way as the Ag^+ concentration. PVP was found to have the two roles, reductant and capping agent, in the photocatalytic systems, and TiO_2 may serve as an electron donor to recover the PVP molecules oxidized by Ag^+. Increasing the PVP content up to ~50 wt % improves the reducing capability of the system, and larger Ag nanoplates resulted from the selective capping of PVP on the {100} facets of Ag. Even higher PVP contents cause random capping and isotropic growth of the different Ag facets, leading to the formation of larger Ag polyhedrons. As for SERS capability, the EF is affected by the morphology of the Ag NCs and is dependent on the synthetic parameter. The highest EF was found for the SERS substrates prepared in the presence of a proper amount of PVP.

■ ASSOCIATED CONTENT

Ⓢ Supporting Information

Degradation kinetics of methyl orange over TiO_2 photocatalysts under UV irradiation; SEM images of Ag NCs grown on rutile in the presence of PVP; PL/PLE spectra of a PVP solution and the supernatant of a PVP/brookite suspension after UV irradiation; relationships between Ag NCs morphologies and processing parameters; and Raman spectra of brookite, rutile, a 0.1 M R6G solution, a 0.1 mM R6G with irradiated PVP mixture solution, and R6G molecules adsorbed on SERS substrates. This material is available free of charge via the Internet at http://pubs.acs.org.

■ AUTHOR INFORMATION

Corresponding Authors

*(J.-G.L.) Tel: +81 29 860 4394; E-mail: LI.Jiguang@nims.go.jp.
*(X.S.) Tel: +86 24 83691566; E-mail: xdsun@mail.neu.edu.cn.

Notes

The authors declare no competing financial interest.

■ ACKNOWLEDGMENTS

T.-L.G. was funded by the China Scholarship Council (grant no. 201206080030) during this work. We are grateful to the Materials Analysis Station and Materials Nanoarchitectonics (MANA) of the National Institute for Materials Science (NIMS) for allowing access to the analysis facilities. Supported by the Joint Funds of the National Natural Science Foundation of China (Grant No. U1302272) and the fund of the State Key Laboratory of Advanced Technologies for Comprehensive Utilization of Platinum Metals (SKL-SPM-201206 and SKM-SPM-201214).

■ REFERENCES

(1) Fleischmann, M.; Hendra, P. J.; McQuillan, A. J. *Chem. Phys. Lett.* **1974**, *26*, 163−166.
(2) Kneipp, K.; Kneipp, H.; Itzkan, L.; Dasari, R. R.; Feld, M. S. *Chem. Rev.* **1999**, *99*, 2957−2976.
(3) Zhang, X. Y.; Young, M. A.; Lyandres, O.; Van Duyne, P. V. *J. Am. Chem. Soc.* **2005**, *127*, 4484−4489.
(4) Levin, C. S.; Bishnoi, S. W.; Grady, N. K.; Halas, N. J. *Anal. Chem.* **2006**, *78*, 3277−3281.
(5) Lee, J. H.; Mahmoud, M. A.; Sitterle, V.; Sitterle, J.; Meredith, J. C. *J. Am. Chem. Soc.* **2009**, *131*, 5048−5049.
(6) Chen, L. M.; Luo, L. B.; Chen, Z. H.; Zhang, M. L.; Zapien, J. A.; Lee, C. S.; Lee, S. T. *J. Phys. Chem. C* **2010**, *114*, 93−100.
(7) Moskovits, M. *Rev. Mod. Phys.* **1985**, *57*, 783−826.
(8) Kim, K. L.; Lee, S. J.; Kim, K. *J. Phys. Chem. B* **2004**, *108*, 9216−9220.
(9) Nie, S.; Emory, S. R. *Science* **1997**, *275*, 1102−1106.
(10) Kleinman, S. L.; Ringe, E.; Valley, N.; Wustholz, K. L.; Phillips, E.; Scheidt, K. A.; Schatz, G. C.; Van Duyne, R. P. *J. Am. Chem. Soc.* **2011**, *133*, 4115−4122.

(11) Camden, J. P.; Dieringer, J. A.; Zhao, J.; Van Duyne, R. P. *Acc. Chem. Res.* **2008**, *41*, 1653−1661.
(12) Fang, Y.; Seong, N.; Dlott, D. D. *Science* **2008**, *321*, 388−392.
(13) Gratton, S. E. A.; Williams, S. S.; Napier, M. E.; Pohlhaus, P. D.; Zhou, Z.; Wiles, K. B.; Maynor, B. W.; Shen, C.; Olafsen, T.; Samulski, E. T.; DeSimone, J. M. *Acc. Chem. Res.* **2008**, *41*, 1685−1695.
(14) Alexander, K. D.; Hampton, M. J.; Zhang, S.; Dhawan, A.; Xu, H.; Lopeza, R. *J. Raman Spectrosc.* **2009**, *40*, 2171−2175.
(15) Hu, M.; Ou, F. S.; Wu, W.; Naumov, I.; Li, X.; Bratkovsky, A. M.; Williams, R. S.; Li, Z. *J. Am. Chem. Soc.* **2010**, *132*, 12820−12822.
(16) Ou, F. S.; Hu, M.; Naumov, I.; Kim, A.; Wu, W.; Bratkovsky, A. M.; Li, X.; Williams, R. S.; Li, Z. *Nano Lett.* **2011**, *11*, 2538−2542.
(17) Wisitsoraat, A.; Tuantranont, A.; Comini, E.; Sberveglieri, G.; Wlodarski, W. *Thin Solid Films* **2009**, *517*, 2775−2780.
(18) Hoffmann, M.R.; Martin, S.T.; Choi, W.; Bahnemann, D.W. *Chem. Rev.* **1995**, *95*, 69−96.
(19) Wang, Y.; Huang, Y.; Ho, W.; Zhang, L.; Zou, Z.; Lee, S. *J. Hazard. Mater.* **2009**, *169*, 77−87.
(20) Su, C.; Tseng, C.-M.; Chen, L.-F.; You, B.-H.; Hsu, B.-C.; Chen, S.-S. *Thin Solid Films* **2006**, *498*, 259−265.
(21) Yang, L. B.; Jiang, X.; Ruan, W. D.; Zhao, B.; Xu, W. Q.; Lombardi, J. R. *J. Phys. Chem. C* **2008**, *112*, 20095−20098.
(22) Yang, L. B.; Jiang, X.; Ruan, W. D.; Yang, J.X.; Zhao, B.; Xu, W. Q.; Lombardi, J. R. *J. Phys. Chem. C* **2009**, *113*, 16226−16231.
(23) Roguska, A.; Kudelski, A.; Pisarek, M.; Opara, M.; Janik-Czachor, M. *Appl. Surf. Sci.* **2011**, *257*, 8182−8189.
(24) Roguska, A.; Kudelski, A.; Pisarek, M.; Lewandowska, M.; Dolata, M.; Janik-Czachor, M. *J. Raman Spectrosc.* **2009**, *40*, 1652−1656.
(25) Huang, Y. X.; Sun, L.; Xie, K. P.; Lai, Y. K.; Liu, B. J.; Ren, B.; Lin, C. J. *J. Raman Spectrosc.* **2011**, *42*, 986−991.
(26) Wang, R. C.; Gao, Y. S.; Chen, S. J. *Nanotechnology* **2009**, *20*, 375605−375610.
(27) Gross, P. A.; Pronkin, S. N.; Cottineau, T.; Keller, N.; Keller, V.; Savinova, E. R. *Catal. Today* **2012**, *189*, 93−100.
(28) Hong, Z. C.; Perevedentseva, E.; Treschev, S.; Wang, J. B.; Cheng, C. L. *J. Raman Spectrosc.* **2009**, *40*, 1016−1022.
(29) Diebold, U. *Surf. Sci. Rep.* **2003**, *48*, 53−229.
(30) Gong, X.; Selloni, A. *J. Phys. Chem. B* **2005**, *109*, 19560−19562.
(31) Liu, M.; Piao, L.Y.; Zhao, L.; Ju, S. T.; Yan, Z. J.; He, T.; Zhou, C. L.; Wang, W. J. *Chem. Commun.* **2010**, *46*, 1664−1666.
(32) Ye, L.; Mao, J.; Liu, J.; Jiang, Z.; Peng, T.; Zan, L. *J. Mater. Chem. A* **2013**, *1*, 10532−10537.
(33) Xu, H.; Ouyang, S.; Li, P.; Kako, T.; Ye, J. *ACS Appl. Mater. Interfaces* **2013**, *5*, 1348−1354.
(34) Liu, L.; Gu, X.; Ji, Z.; Zou, W.; Tang, C.; Gao, F.; Dong, L. *J. Phys. Chem. C* **2013**, *117*, 18578−18587.
(35) Li, D. W.; Pan, L. J.; Li, S.; Liu, K.; Wu, S. F.; Peng, W. *J. Phys. Chem. C* **2013**, *117*, 6861−6871.
(36) Es-Souni, M.; Habouti, S.; Pfeiffer, N.; Lahmar, A.; Dietze, M.; Solterbeck, C.-H. *Adv. Funct. Mater.* **2010**, *20*, 377−385.
(37) Li, J.-G.; Tang, C.; Li, D.; Haneda, H.; Ishigaki, T. *J. Am. Ceram. Soc.* **2004**, *87*, 1358−1361.
(38) Li, J.-G.; Ishigaki, T.; Sun, X. *J. Phys. Chem. C* **2007**, *111*, 4969−4976.
(39) Ohtani, B.; Handa, J.; Nishimoto, S.; Kagiya, T. *Chem. Phys. Lett.* **1985**, *120*, 292−294.
(40) Kominami, H.; Kohno, M.; Kera, Y. *J. Mater. Chem.* **2000**, *10*, 1151−1156.
(41) Zhang, J. M.; Ma, F.; Xu, K. W. *Appl. Surf. Sci.* **2004**, *229*, 34−42.
(42) Wang, Z. L. *J. Phys. Chem. B* **2000**, *104*, 1153−1175.
(43) Xiong, Y.; Xia, Y. *Adv. Mater.* **2007**, *19*, 3385−3391.
(44) Lofton, C.; Sigmund, W. *Adv. Funct. Mater.* **2005**, *15*, 1197−1208.
(45) Elechiguerra, J. L.; Reyes-Gasga, J.; Yacaman, M. J. *J. Mater. Chem.* **2006**, *16*, 3906−3919.
(46) Hofmeister, H.; Nepijko, S. A.; Levlev, D. N.; Schulze, W.; Ertl, G. *J. Cryst. Growth* **2002**, *234*, 773−781.
(47) Nepijko, S. A.; Levlev, D. N.; Schulze, W.; Urban, J.; Ertl, G. *ChemPhysChem* **2000**, *1*, 140−142.
(48) Baletto, F.; Ferrando, R. *Phys. Rev. B* **2001**, *63*, 155408−155418.
(49) Baletto, F.; Ferrando, R.; Fortunelli, A.; Montalenti, F.; Mottet, C. *J. Chem. Phys.* **2002**, *116*, 3856−3864.
(50) Baletto, F.; Ferrando, R. *Rev. Mod. Phys.* **2005**, *77*, 371−423.
(51) Cleveland, C.; Landman, U. *J. Chem. Phys.* **1991**, *94*, 7376−7397.
(52) Kirkland, A. I.; Jefferson, D. A.; Duff, D. G.; Edwards, P. P.; Gameson, I.; Johnson, B. F. G.; Smith, D. J. *Proc. R. Soc. London, Ser. A* **1993**, *440*, 589−609.
(53) Germain, V.; Li, J.; Ingert, D.; Wang, Z. L.; Pileni, M. P. *J. Phys. Chem. B* **2003**, *107*, 8717−8720.
(54) Washio, I.; Xiong, Y.; Yin, Y.; Xia, Y. *Adv. Mater.* **2006**, *18*, 1745−1749.
(55) Sun, Y.; Xia, Y. *Science* **2002**, *298*, 2176−2179.
(56) Xiong, Y.; Chen, J.; Wiley, B.; Xia, Y.; Yin, Y.; Li, Z. Y. *Nano Lett.* **2005**, *5*, 1237−1242.
(57) Ding, X.; Kan, C.; Mo, B.; Ke, S.; Cong, B.; Xu, L.; Zhu, J. *J. Nanopart. Res.* **2012**, *14*, 1000−1009.
(58) Wiley, B.; Sun, Y.; Mayers, B.; Xia, Y. *Chem.—Eur. J.* **2005**, *11*, 454−463.
(59) Kirkland, A. I.; Jefferson, D. A.; Duff, D. G.; Edwards, P. P.; Gameson, I.; Johnson, B. F. G.; Smith, D. J. *Proc. R. Soc. London, Ser. A* **1993**, *440*, 589−609.
(60) Wiley, B. J.; Im, S. H.; Li, Z. Y.; McLellan, J.; Siekkinen, A.; Xia, Y. *J. Phys. Chem. B* **2006**, *110*, 15666−15675.
(61) Song, W.; Wang, Y.; Zhao, B. *J. Phys. Chem. C* **2007**, *111*, 12786−12791.
(62) Pisarek, M.; Roguska, A.; Kudelski, A.; Andrzejczuk, M.; Janik-Czachor, M.; Kurzydłowski, K. J. *Mater. Chem. Phys.* **2013**, *139*, 55−65.